3-D Wireless Power Transfer With Orthogonal Transmitters and Adaptive MPC-MPPT

Zhenxing Ye, *Student Member, IEEE*, Ka Wai Eric Cheng, *Fellow, IEEE*, Ka Wing Chan, *Member, IEEE*, and Siu Wing Or

***Abstract*—This article presents a three-dimensional wireless power transfer system that uses three transmitting coils oriented in orthogonal directions and an adaptive model predictive control (MPC) strategy that incorporates maximum power point tracking (MPPT). The framework combines MPC's predictive optimization and MPPT's efficiency-seeking behavior, which simultaneously optimizes power tracking accuracy, system efficiency, and current distribution, while maintaining zero-voltage-switching operation. The dynamic weight-adjustment mechanism alters the weights of competing objectives automatically and based on the current operational conditions. The system model indicates that power distribution in 3-D space fits a Lemniscate of Bernoulli surface revolved about its longitudinal axis, so the rotational Lemniscate of Bernoulli surface is important to the control design. The experimental results presented in this article show up to 20% increased efficiency at 40 cm transmission distance, and a peak efficiency of 87% at 60 W and at 40 cm × 40 cm × 40 cm charging volume. The framework provides stable power delivery while the receiver is in motion, making it appealing for applications that require spatial freedom, including mobile robots and bio-inspired aerial vehicles.**

***Index Terms*—Adaptive control, maximum power point tracking (MPPT), model predictive control (MPC), wireless power transfer (WPT).**

I. INTRODUCTION

WIRELESS power transfer (WPT) systems based on magnetic resonance coupling have shown significant potential in various applications, from consumer electronics charging to electric vehicle powering [1], [2], [3]. A critical challenge in WPT systems lies in maintaining optimal power transfer efficiency while ensuring stable power delivery, particularly in three-dimensional (3-D) space where coupling conditions vary continuously [4], [5], [6], [7], [8]. This challenge becomes more pronounced in applications such as bio-inspired micro aerial vehicles, where the power receiver's position and orientation change dynamically during operation.

A critical challenge in three-dimensional wireless power transfer (3-D-WPT) systems lies in maintaining optimal power transfer efficiency while ensuring stable power delivery, particularly in three-dimensional space where coupling conditions vary continuously [9], [10], [11]. Without effective control optimization, efficiency variations can exceed 30% as receivers move freely within the charging volume. This is especially problematic for applications requiring consistent power delivery despite spatial movement, such as mobile robots, biomedical implants, and bio-inspired aerial vehicles [12], [13], [14].

Several approaches have been proposed to address the challenges in 3-D-WPT systems. One common solution involves utilizing specialized compensation networks to improve coupling robustness [15], [16], [17]. However, these passive approaches cannot adapt dynamically to rapid position changes and often result in suboptimal efficiency across the charging volume. Other researchers have explored multicoil arrays to enhance spatial coverage [18], [19], [20], but these typically require complex switching mechanisms and suffer from significant cross-coupling interference. Dome and cavity-based structures [21] offer another approach, providing omnidirectional charging capability but with limited efficiency at longer distances.

Control strategies have also been investigated to optimize WPT performance in dynamic environments. Model predictive control (MPC) has demonstrated advantages in managing WPT systems by anticipating coupling variations [22], [23], [24], while maximum power point tracking (MPPT) techniques have been applied to maximize efficiency under varying conditions [25], [26]. However, these approaches have primarily been implemented separately, focusing either on power regulation or efficiency optimization, but rarely addressing both simultaneously in 3-D applications.

Recent developments in magnetic field projection and current phase control [27] have provided new methods for shaping magnetic fields in 3-D space, but these typically require precise receiver position information, which is challenging to obtain in practical applications. Similarly, sensing intermediate coils have been proposed for receiver position identification [28], but these approaches increase system complexity and cost.

As shown in Fig. 1, this article implements the proposed control strategy on a 3-D-WPT system featuring three square-shaped transmitting coils (Coil A, Coil B, and Coil C) positioned orthogonally along the x, y, and z axes, creating

---

Received 4 June 2025; revised 12 September 2025; accepted 8 October 2025. Date of publication 13 October 2025; date of current version 19 January 2026. This work was supported by the Research Grant Council under Project 15207721 and Project 15225422. Recommended for publication by Associate Editor B. Lee. *(Corresponding author: Ka Wai Eric Cheng.)*

Zhenxing Ye, Ka Wing Chan, and Siu Wing Or are with the Department of Electrical and Electronic Engineering, The Hong Kong Polytechnic University, Hong Kong (e-mail: zhenxing-chris.ye@connect.polyu.hk; eeswor@polyu.edu.hk; eeswor@polyu.edu.hk).

Ka Wai Eric Cheng was with Hong Kong Polytechnic University, Hong Kong. He is now with the University of California, Merced, CA 95343 USA (e-mail: ericcheng@ucmerced.edu).

Color versions of one or more figures in this article are available at https://doi.org/10.1109/TPEL.2025.3621141.

Digital Object Identifier 10.1109/TPEL.2025.3621141

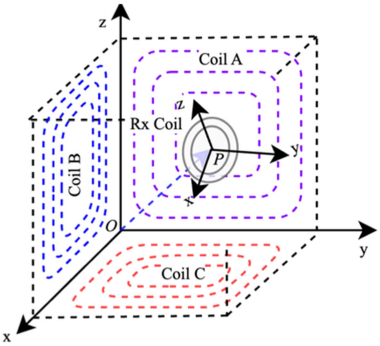

Fig. 1. Schematic diagram illustrating the fundamental principles of 3-D-WPT.

a three-dimensional magnetic field distribution. This arrangement, coupled with a circular receiving coil, enables power transfer with six degrees of freedom within the charging volume. While the physical structure provides the foundation, the core contribution of this work lies in the development of an advanced control strategy that optimizes the operation of this multicoil system.

This article presents a novel control approach for 3-D-WPT systems that integrates adaptive MPC with MPPT capabilities. The key contributions include the following.

1) Development of a system architecture using three-square transmitting coils orthogonally spaced to construct a controllable three-dimensional magnetic field distribution, allowing the receiver to transfer power from all positions and directions within the charging volume.
2) Implementation of a control scheme combining MPC with MPPT, while simultaneously handling both power regulation and efficiency improvement to alleviate the shortcomings of traditional controllers from varying conditions of spatial coupling in the charging case.
3) Creation of a cost function parameterized to allow for the objective of efficiency improvement, power tracking accuracy, and switching conditions resulting in multiple objectives to be optimized by *J*(*k*).
4) Ability to automatically adjust the weight coefficient values of the cost function $w_1(k)$, $w_2(k)$, and $w_3(k)$that relates to the operational state. It allows to prioritize power tracking if insufficient power is generated and ensure is has zero-voltage-switching (ZVS) condition under any time switching condition identified by auto-wake conditions.

II. PROPOSED SYSTEM AND CHARGING ANALYSIS

This section presents a comprehensive analysis of the proposed 3-D-WPT system, focusing on its unique configuration, operating principles, and mathematical characterization of power distribution in 3-D space.

A. System Configuration and Circuit Analysis

The proposed 3-D-WPT system consists of three mutually orthogonal square-shaped transmitting coils (aligned along the *x*-, *y*-, and *z*-axes) and a circular receiving coil with arbitrary orientation in three-dimensional space. Each transmitting branch employs a series-series compensation topology, as illustrated in Fig. 2.

Fig. 2 illustrates the comprehensive schematic of the proposed 3-D-WPT system. The system architecture consists of three independent inverter circuits (Inverters A, B, and C) that drive three orthogonally arranged transmitting coils (Coils A, B, and C). Each inverter utilizes four MOSFETS (S1–S12) controlled by dedicated drivers. The power transmission is regulated by a DSP controller (TMS320F28335) that processes feedback from voltage and current sensors through ADC channels. The transmitting coils generate a 3-D magnetic field that energizes the receiving circuit, which includes a tuned resonant network (L_{rx} and C_{rx}), rectification circuit (Q_1–Q_4), and output filtering (Co) that delivers power to the load (R_{Load}). This configuration enables efficient wireless power delivery regardless of the receiver's orientation in 3-D space.

Fig. 3 presents the equivalent circuit model of the 3-D-WPT system. In this model, the three transmitting branches are represented by their respective voltage sources (U_A, U_B, U_C), series compensation capacitors ($C_{txA}, C_{txA}, C_{txC}$), transmitting coils ($L_{txA}$, L_{txB}, L_{txC}) with their associated resistances (R_A, R_B, R_C), and the mutual inductances (M_A, M_B, M_C) coupling to the receiving coil. The receiving circuit is composed of the receiver inductance (L_{rx}), resonant capacitor (C_{rx}), coil resistance (R_{Rx}), and the equivalent load resistance (R_{Load}). The circuit model enables precise analysis of the system's power transfer capabilities in three-dimensional space.

The fundamental harmonics approximation method is used to analyze the proposed WPT system. The fundamental component of the output voltage of the inverter is given as

$$U_i = \frac{2\sqrt{2}}{\pi} U_{dc} \sin\frac{\phi_i}{2} \angle 0^\circ, i \ = \ A, B, C \tag{1}$$

where ϕ_A, ϕ_B, and ϕ_C are the phase-shift angles for each transmitting branch, serving as the primary control variables for optimizing power transfer.

The equivalent rms value of the rectifier input voltage U_{rx} can be described as

$$U_{rx} = \frac{2\sqrt{2}}{\pi} U_0 \tag{2}$$

where U_0 is the output voltage on the load. R_{eq} is the input equivalent load of the rectifier that can be derived as

$$R_{eq} = \frac{8}{\pi^2} R_L. \tag{3}$$

Using complex phasor representation, the circuit equations are as

$$\begin{bmatrix} U_A \\ U_B \\ U_C \\ 0 \end{bmatrix} = \begin{bmatrix} Z_{txA} & 0 & 0 & j\omega M_A \\ 0 & Z_{txB} & 0 & j\omega M_B \\ 0 & 0 & Z_{txC} & j\omega M_C \\ j\omega M_A & j\omega M_B & j\omega M_C & Z_{rx} \end{bmatrix} \begin{bmatrix} I_{txA} \\ I_{txB} \\ I_{txC} \\ I_{rx} \end{bmatrix} \tag{4}$$

where $Z_{txi} = \ j\omega L_{txi} + 1/j\omega C_{txi} + R_i$, $Z_{rx} = \ j\omega L_{rx} + 1/j\omega C_{rx} + R_{rx} + R_{\mathrm{eq}}$.

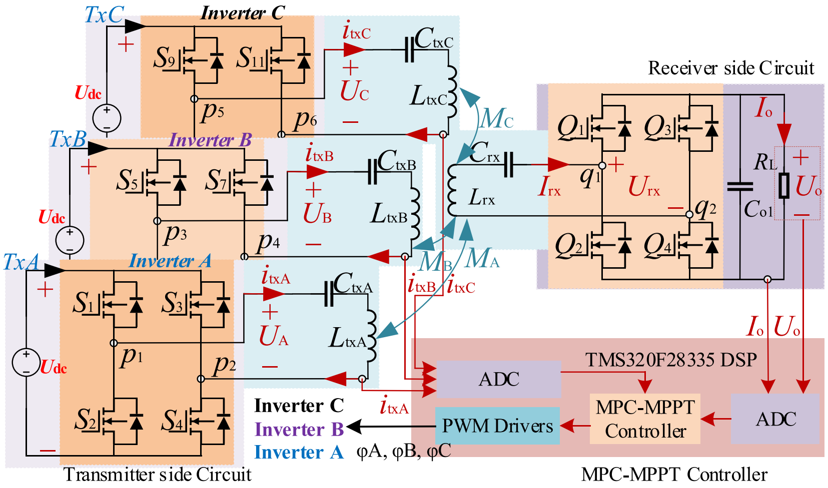

Fig. 2. Proposed schematic of the 3-D-WPT system.

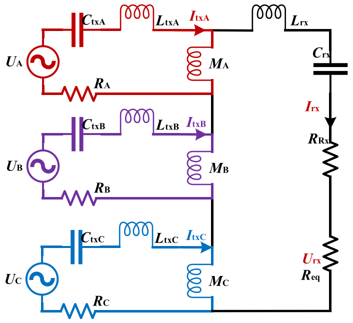

Fig. 3. Equivalent circuit of the 3-D-WPT system.

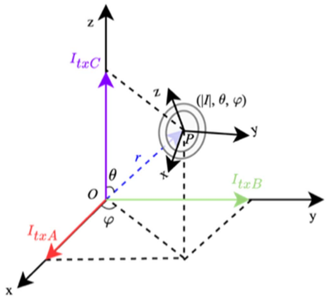

Fig. 4. Amplitude modulation description of current I_{txA}, I_{txB}, and I_{txC}.

At resonant frequency $\omega = 1/\sqrt{L_{tx}C_{tx}} = 1/\sqrt{L_{rx}C_{rx}}$, these equations simplify to

$$\begin{bmatrix} U_A \\ U_B \\ U_C \\ 0 \end{bmatrix} = \begin{bmatrix} R_A & 0 & 0 & j\omega M_A \\ 0 & R_B & 0 & j\omega M_B \\ 0 & 0 & R_C & j\omega M_C \\ j\omega M_A & j\omega M_B & j\omega M_C & R_{rx} + R_{Load} \end{bmatrix} \begin{bmatrix} I_{txA} \\ I_{txB} \\ I_{txC} \\ I_{rx} \end{bmatrix}. \tag{5}$$

The three transmitter coils are fed with ac current sources I_{txA}, I_{txB}, and I_{txC} through current control at the same frequency that defines the rotating frequency of the resultant magnetic field. For genuine omnidirectional WPT, nonidentical current control must be adopted [6], [11], [12]. Based on the current amplitude control [12], the three currents in the three transmitter coils are set as

$$\begin{bmatrix} I_{txA} \\ I_{txB} \\ I_{txC} \end{bmatrix} = \begin{bmatrix} I\sin\theta\cos\varphi \\ I\sin\theta\sin\varphi \\ I\cos\theta \end{bmatrix} \tag{6}$$

where θ and φ are the angles related to the resultant current vector in a spherical coordinate system, as shown in Fig. 4, and $\boldsymbol{I}$ is a sinusoidal time function.

This representation is particularly well suited for omnidirectional WPT, since the $(\sin\theta\cos\varphi)^2 + (\sin\theta\sin\varphi)^2 + (\cos\theta\,)^2 = 1$, enabling true omnidirectional power transfer capability. The current representation in spherical coordinates offers significant control advantages: simplifies the optimization process by reducing control dimensionality; provides intuitive directional control of the magnetic field; enables efficient exploration of the entire 3-D space through systematic variation of θ and φ; and facilitates the implementation of adaptive control strategies based on receiver position.

B. Mutual Inductance Analysis in 3-D Space

To characterize the six-degree-of-freedom coupling with fidelity suitable for control synthesis, a three-dimensional magneto–quasi-static finite-element model was constructed to mirror the prototype geometry, winding arrangement, and material properties. At the operating frequency of 85 kHz, each of the three orthogonal transmitter coils was excited individually with a unit sinusoidal current while the receiver coil was scanned over the defined workspace in position and orientation; the resulting flux linkage was extracted to compute the mutual inductance field. The spatial map reported in Fig. 5 is directly obtained from this dataset after routine mesh-refinement and domain-size sensitivity checks confirmed numerical convergence; the mutual inductance values show a nonlinear fluctuating structure with the change of coil attitude or position. The mutual inductance values range from 0.9 to 4.8 μH. This physics-based map serves as the ground truth for subsequent controller-oriented approximation.

Based on the current simulation results, the data will be analyzed and fitted to derive a spatial distribution function for the mutual inductance between the square transmit coil and the circular receive coil. The mutual inductance distribution

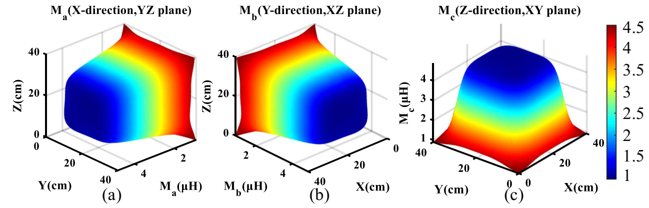

Fig. 5. Mutual inductance distribution of transmitter-receiver coils in three dimensions. (a) $M_A(x,y,z)$. (b) $M_B(x,y,z)$. (c) $M_C(x,y,z)$.

function is approximated by the following formula:

$$\begin{cases} M_A\ (x,y,z) = M_0\ + \frac{\Delta M}{1+e^{\left(\alpha_1 R_{sqA}(P_1,P_2)-\alpha_2\right)}} \\ M_B\ (x,y,z) = M_0\ + \frac{\Delta M}{1+e^{\left(\alpha_1 R_{sqB}(P_1,P_2)-\alpha_2\right)}} \\ M_C\ (x,y,z) = M_0\ + \frac{\Delta M}{1+e^{\left(\alpha_1 R_{sqC}(P_1,P_2)-\alpha_2\right)}} \end{cases},$$

$$\begin{cases} x = r\sin\theta\cos\varphi \\ y = r\sin\theta\sin\varphi \\ z = r\cos\theta \\ x^2+y^2+\ z^2 = r^2 \end{cases} \tag{7}$$

where $(P_1,\ P_2)$ are two coordinate variables in the projection plane, $R_{sqA,B,C}\ \ (P_1,\ P_2) =\ \ (|P_1-P_c|^n+|P_2-P_c|^n)^{1/n}$, $P_c =\ 20$ is the center of each face, $M_0$is the base mutual inductance value 0.9, ΔM is the amount of mutual inductance variation 3.9, α_1 and α_2 are the variation excess parameters 0.7 and 16.5 respectively, and n is the shape parameter 4, r is the distance from point $\boldsymbol{O}$ to the center $\boldsymbol{P}$ of the receiving coil. Equation (7) is derived as a compact surrogate of the FEM-generated mutual inductance field through normalization and parametric approximation, with the explicit aim of providing a differentiable, low-complexity representation amenable to real-time optimization. The constants 0.9, 3.9, 0.7, and 16.5 are identified by a weighted nonlinear least-squares procedure over the FEM samples; they reflect, respectively, amplitude scaling, axial anisotropy, radial decay shaping, and the far-field transition scale inherent to the coil geometry. The above-mentioned equation describes the general mutual inductance trend from the square transmitting coil to the circular receiving coil by the projection method, and the analysis helps to characterize the coupling relationship effectively at different positions.

C. Power Distribution and Analysis of the Proposed 3-D-WPT System

At the resonant frequency, the current at the receiving end can be expressed as

$$I_{rx} = -\frac{j\omega}{R_{rx}+R_{\text{eq}}}\left(M_A I_{txA} + M_B I_{txB} + M_C I_{txC}\right). \tag{8}$$

Substituting the spherical coordinate system current expression gives

$$I_{rx} = -\frac{j\omega I\left(M_A \sin\theta\cos\varphi + M_B\sin\theta\sin\varphi + M_C\cos\theta\right)}{R_{rx}+R_{\text{eq}}}. \tag{9}$$

The load power can be calculated as

$$\begin{aligned} P_{\text{load}} &= \left|I_{rx}\right|^2 R_{\text{eq}} \\ &= \frac{\omega^2 I^2 R_{\text{eq}}(M_A\sin\theta\cos\varphi + M_B\sin\theta\sin\varphi + M_C\cos\theta)^2}{(R_{rx}+R_{\text{eq}})^2}. \end{aligned} \tag{10}$$

This power expression can be further expanded and simplified using trigonometric identities (11) as shown at the bottom of this page, where

$$\gamma_{3D} =\ \arctan\frac{M_C}{\sqrt{M_A^2+M_B^2}\sin\left(\arctan\frac{M_A}{M_B}+\varphi\right)} \tag{12}$$

$$K_{3\text{D}}(\varphi) = \frac{\omega^2\left[\left(M_A^2+M_B^2\right)\sin^2\left(\arctan\frac{M_A}{M_B}+\varphi\right)+M_C^2\right]}{(R_{rx}+R_{\text{eq}})^2}. \tag{13}$$

Power distribution can be characterized by its maximum and minimum values. The maximum power condition occurs when

$$\arctan\frac{M_A}{M_B}+\varphi\ =\frac{\pi}{2}\ \text{and}\ \gamma_{3\text{D}}+\theta\ =\frac{\pi}{2}\,. \tag{14}$$

Under these conditions, the maximum load power is

$$P_{\text{load}_{\text{max}}} = I^2\ K_{3\text{D}}R_{\text{eq}}. \tag{15}$$

The minimum power condition occurs when $\gamma_{3\text{D}}+\theta\ =\ 0$, resulting in

$$P_{\text{load}_{\text{min}}} =\ 0. \tag{16}$$

The output power is

$$P_{\text{out}} = I_{rx}^2\ R_{rx} + I_{rx}^2\ R_{eq} = I^2\ R_{rx} + R_{\text{eq}}K_{3\text{D}}\varphi\sin^2\gamma_{3\text{D}}+\theta. \tag{17}$$

The total input power of the system is

$$P_{\text{in}} = \sum_{i=A,B,C} I_{txi}^2 R_i\ + I_{rx}^2\left(R_{rx}+R_{\text{eq}}\right). \tag{18}$$

When $R_A = R_B\ = R_C\ =\ R$, the input power is

$$P_{\text{in}} = I^2\ R + I^2\left(R_{rx}+R_{\text{eq}}\right)K_{3\text{D}}\left(\varphi\right)\sin^2\left(\gamma_{3\text{D}}+\theta\right). \tag{19}$$

The input power is at the maximum value condition

$$P_{\text{in}_{\text{max}}} = I^2\ R + I^2 K_{3\text{D}}\left(R_{rx}+R_{\text{eq}}\right). \tag{20}$$

Under the minimum value condition is

$$P_{\text{in}_{\text{min}}} = I^2\ R. \tag{21}$$

$$P_{\text{load}} = \frac{\omega^2 I^2 R_{\text{eq}}\left(\left(M_A^2+M_B^2\right)\times\sin^2\left(\arctan\frac{M_A}{M_B}+\varphi\right)\sin^2\theta + M_C^2\cos^2\theta\right)}{(R_{rx}+R_{eq})^2} = I^2\ R_{\text{eq}}K_{3\text{D}}\left(\varphi\right)\sin^2\left(\gamma_{3\text{D}}+\theta\right) \tag{11}$$

This comprehensive mathematical characterization of power distribution provides the theoretical foundation for developing advanced control strategies that can navigate this three-dimensional power landscape to achieve optimal performance regardless of receiver position.

III. ADAPTIVE MPC STRATEGY WITH INTEGRATED MPPT

This section develops an adaptive MPC method that integrates MPPT, improving efficiency, stabilizing load power, and sustaining the ZVS margin. The controller leverages the resonant equivalent model as a practical constraint for feasible operation. In physical pursuit of determining a suitable short-term physical predictive task, a spherical candidate set of maneuvers is used for directional alignment and phase alignment coupled with mode shape representing positions. This will materialize into consistent determination of "magnetic field orientation-phase-shift modulation-power/efficiency-soft-switching" despite unknown poses and rapid coupling transitions.

A. Implementation of MPC

In the proposed MPC framework, the system states at a discrete time step *k* are defined as the vector

$$x\ (k) = \left[I_{txA}\left(k\right), I_{txB}\left(k\right), I_{txC}\left(k\right), \theta\left(k\right), \varphi\left(k\right)\right]^T \tag{22}$$

which includes the currents of three transmitting coils and two angular parameters in the spherical coordinate system. The control variables are defined as the phase shift angles of three inverters

$$u\ (k) = \left[\phi_A\left(k\right), \phi_B\left(k\right), \phi_C\left(k\right)\right]^T \tag{23}$$

and the system outputs include load power and transmission efficiency

$$y\ (k) = \left[P_{\text{load}}\left(k\right), \eta\left(k\right)\right]^T. \tag{24}$$

According to the circuit relationships analyzed in Section II, there exists a clear mapping between inverter phase shift angles and coil currents

$$I_{txi}\ (k) = \frac{U_{\text{dc}}}{\pi R}\sin\phi_i\left(k\right), i\ =\ A, B, C. \tag{25}$$

These currents can simultaneously be represented as directional vectors in the spherical coordinate system

$$\begin{bmatrix} I_{txA}\left(k\right) \\ I_{txB}\left(k\right) \\ I_{txC}\left(k\right) \end{bmatrix} = \begin{bmatrix} I\sin\theta\left(k\right)\cos\varphi\left(k\right) \\ I\sin\theta\left(k\right)\sin\varphi\left(k\right) \\ I\cos\theta\left(k\right) \end{bmatrix} \tag{26}$$

where ***I*** represents the magnitude of the current vector. This representation establishes a bidirectional mapping from control variables $u(k)$ to spherical coordinate angles $\theta(k)$ and $\varphi(k)$, providing the mathematical foundation for the MPC prediction process.

The core of the MPC algorithm is to predict system behavior within both the prediction horizon N_p and the control horizon N_c, At time step *k*+*i* (where $i = 1, 2, \ldots, N_p$), MPC needs to calculate the predicted outputs $\{y(k+i)\}_{i\,=\,1}^{N_p}$ under candidate control sequences $\{u(k+i-1)\}_{i\,=\,1}^{N_c}$. The prediction process first converts candidate control variables $u(k+i-1)$ to corresponding $\theta(k+i)$ and $\varphi(k+i)$, then calculates key parameters $K_{\text{3D}}(\varphi(k+i))$ and $\gamma_{\text{3D}}(k+i)$. These two parameters characterize the coupling relationship between magnetic field direction and receiver position, with calculation formulas as follows:

$$K_{\text{3D}}\ \left(\varphi\left(k+i\right)\right) = \frac{\omega^2\left[\left(M_A^2+M_B^2\right)\sin^2\left(\arctan\frac{M_A}{M_B}+\varphi\left(k+i\right)\right)+M_C^2\right]}{\left(R_{rx}+R_{\text{eq}}\right)^2} \tag{27}$$

$$\gamma_{\text{3D}}\ \left(k+i\right) = \arctan\frac{M_C}{\sqrt{M_A^2+M_B^2}\sin\left(\arctan\frac{M_A}{M_B}+\varphi\left(k+i\right)\right)}. \tag{28}$$

Based on these parameters, the system further predicts load power

$$P_{\text{load}}\left(k+i\right) = I^2 R_{\text{eq}} K_{\text{3D}}\left(\varphi\left(k+i\right)\right) \times\sin^2\left(\gamma_{\text{3D}}\left(k+i\right)+\theta\left(k+i\right)\right) \tag{29}$$

and system efficiency

$$\eta\left(k+i\right) = \frac{R_{\text{eq}}K_{\text{3D}}\left(\varphi\left(k+i\right)\right)\sin^2\left(\gamma_{\text{3D}}\left(k+i\right)+\theta\left(k+i\right)\right)}{R+\left(R_{rx}+R_{\text{eq}}\right)K_{\text{3D}}\left(\varphi\left(k+i\right)\right)\sin^2\left(\gamma_{\text{3D}}\left(k+i\right)+\theta\left(k+i\right)\right)}. \tag{30}$$

These expressions directly derive from the theoretical analysis in Section II, fully reflecting the influence of control variables (through θ and φ) on system performance. To reduce computational complexity, candidate control sequences are typically selected from a predefined finite set, for example, *N* points uniformly distributed on a sphere, rather than optimizing in continuous space.

The cost function designed in this research integrates three main objectives: maximizing power transfer efficiency, tracking target load power, and ensuring ZVS conditions. This cost function is expressed as

$$J\ (k) = \sum_{i=1}^{N_p}\left[\begin{array}{c} w_1\left(k\right)\left(1-\eta\left(k+i\right)\right)+w_2\left(k\right)\left(1-\frac{P_{\text{load}}\left(k+i\right)}{P_{\text{ref}}}\right) \\ +w_3\left(k\right)J_{\text{ZVS}}\left(k+i\right) \end{array}\right] \tag{31}$$

where $w_1(k)$, $w_2(k)$, and $w_3(k)$ are weight coefficients used to balance the importance of different control objectives; P_{ref} is the reference power, representing the desired load power transfer

$J_{\text{ZVS}}(k+i)$is the ZVS penalty term, defined as

$$J_{\text{ZVS}}\ \left(k+i\right) = \sum_{j=A,B,C}\max\left\{0, I_{\min}-\left|I_{txj}\left(k+i\right)\right|\right\}. \tag{32}$$

Here, $I_{txj}(k+i)$ denotes the predicted fundamental rms current magnitude of the *j*th transmitter branch at step $k+i$ ($j \in \{A,\ B,\ C\}$), and $I_{\min}$ is a calibrated threshold that represents the minimum branch current required to guarantee sufficient energy to charge/discharge the device output capacitances within the dead-time at the fixed operating frequency. Under the resonant, fundamental-harmonic operating assumption, maintaining $|I_{txj}|\geq I_{\min}$ is a sufficient control-level proxy for sustaining ZVS. This penalty term implements the soft inequality $|I_{txj}|\geq I_{\min}$ in hinge form: it vanishes when the ZVS margin is met and increases linearly with the deficit, thereby biasing the optimizer toward candidate actions that preserve ZVS and avoid switching-loss/EMI degradation.

The design of the cost function reflects the multiobjective optimization nature of the system, allowing a balance between power transfer, efficiency, and reliability through appropriate adjustment of weights.

In each control cycle, MPC determines the optimal control sequence by solving the optimization problem

$$u*\ (k:k+N_p-1) = \arg \min_{u(k:k+N_p-1)} J \tag{33}$$

while adhering to control variable constraints $\phi_j(k+i)\in[0,2\pi)$ and ZVS conditions $|I_{txj}(k+i)|\geq I_{\min}$.

The actual solution process first generates a set of N candidate points uniformly distributed on a sphere $\{(\theta_n,\varphi_n)\}_{n=1}^{N}$ then maps each candidate point to corresponding control variables $\{(\phi_A^n,\phi_B^n,\phi_C^n)\}_{n=1}^{N}$, calculates the cost function value for each candidate control sequence, and finally selects the control sequence with the minimum cost function value as the optimal control action. Considering computational resource limitations, a relatively short prediction horizon ($N_p = 3-5$) and an appropriate number of candidate points ($N = 20$–30) are typically set to balance control performance and computational burden.

B. Integrated Design of MPPT and MPC

The fundamental goal of MPPT in 3-D-WPT systems is to locate the maximum power transfer point when the receiver's position and orientation are unknown or changing. Based on the theoretical analysis of the performance presented in Section II, the maximum power transfer condition can be expressed as:$\sin^2(\arctan\frac{M_A}{M_B}+\varphi) = 1$ and $\sin^2(\gamma_{3D}+\theta) = 1$. These expressions establish two critical criteria: 1) the phase alignment between the transmitter's magnetic field and the receiver coil plane, and 2) the real-time adaptive adjustment of the magnetic field direction based on receiver dynamics.

The MPC-MPPT integration method proposed in this research directly incorporates MPPT objectives into the MPC cost function, enabling the controller to pursue multiple objectives simultaneously. By appropriately setting weight coefficients $w_1(k)$, $w_2(k)$, and $w_3(k)$, the system can automatically adjust priorities under different operating conditions. The predictive controller aggregates three physical objectives—efficiency, power tracking, and ZVS robustness—into a single weighted cost and, at each interval, evaluates a finite set of feasible field-orientation/phase-alignment commands that are consistent with resonant operation. The weights $w_1(k)$, $w_2(k)$, and $w_3(k)$ bias this ranking toward higher delivered power, stronger soft-switching margins, or improved efficiency as operating conditions evolve; the explicit adaptive scheduling law and tuned parameters are presented in Section III-C [(37) and Figs. 6 and 7].

To implement the MPC-MPPT integrated algorithm, the system needs to continuously estimate receiver parameters. This research adopts a perturbation-observation-based approach, estimating system states by measuring input power under different control parameters. Input power can be expressed as

$$\begin{aligned} P_{\text{in}}\ (k) &= I^2\ R + I^2\left(R_{rx}+R_{\text{eq}}\right)K_{\text{3D}}\left(\varphi\left(k\right)\right)\\ &\quad\times \sin^2\left(\gamma_{\text{3D}}\left(k\right)+\theta\left(k\right)\right). \end{aligned} \tag{34}$$

By observing power changes under different control conditions, the system can derive mutual inductance coefficients and optimal directions. Specifically, the difference between maximum input power and minimum input power satisfies the relationship

$$P_{\text{in}_{\max}} - P_{\text{in}_{\min}} = I^2\ K_{\text{3D}}\left(R_{rx}+R_{\text{eq}}\right) \tag{35}$$

providing a basis for mutual inductance estimation. Based on the estimated mutual inductance coefficients, the system can calculate the optimal direction

$$\begin{cases} \varphi_{\text{opt}} = \frac{\pi}{2} - arctan\frac{M_A}{M_B} \\ \theta_{\text{opt}} = \frac{\pi}{2} - \gamma_{\text{3D}} \end{cases}. \tag{36}$$

Finally, the system uses the estimated parameters to update the MPC prediction model, completing the adaptive control loop. The resulting priority shifts are operationalized by the adaptive weight adjustment detailed in Section III-C, ensuring consistent behavior under time-varying receiver motion.

C. Adaptive Weight Adjustment Based on Operating Conditions

The proposed MPC-MPPT structure adjusts the cost-function weights $w_1(k)$, $w_2(k)$, and $w_3(k)$ to achieve the best tradeoff among the differing objectives of optimizing efficiency, at the same time attempting to track power and maintain ZVS. The adjustments depend on two operating-state indicators so the controller can appropriately bias these objectives in real time, as dictated by system needs, without using additional sensors or ongoing substantial computational effort.

We use the normalized power-tracking error $\varepsilon P(k) = |P_{\text{load}}(k)-P_{\text{ref}}|/P_{\text{ref}}$ and a ZVS violation indicator $I_{\text{ZVS}}(k)\in\{0,1\}$. Here, $I_{\text{ZVS}}\ (k) = 1$ if any transmitter branch fails to meet the ZVS margin in the current cycle, and $I_{\text{ZVS}}\ (k) = 0$ otherwise. These two quantities are sufficient to determine whether the controller should emphasize power regulation (when $\varepsilon P(k)$ is large), preserve soft switching (when $I_{\text{ZVS}}\ (k) = 1$), or revert to nominal efficiency-oriented operation.

Using these indicators, the weights are updated as follows:

$$\begin{cases} w_1\left(k\right) &= \left[w_{\text{1base}} - \lambda_1\cdot\varepsilon P\left(k\right) + \gamma_1\cdot I_{\text{ZVS}}\left(k\right)\right]/w_{\text{total}}\\ w_2\left(k\right) &= \left[w_{\text{2base}} + \lambda_2\cdot\varepsilon P\left(k\right) - \gamma_2\cdot I_{\text{ZVS}}\left(k\right)\right]/w_{\text{total}}\\ w_3\left(k\right) &= \left[w_{\text{3base}} - \lambda_3\cdot\varepsilon P\left(k\right) + \gamma_3\cdot I_{\text{ZVS}}\left(k\right)\right]/w_{\text{total}} \end{cases} \tag{37}$$

where w_{total} is the total of the three bracketed numerators in (37) and the constraint $w_1(k)+w_2(k)+w_3(k) = 1$ is enforced for each cycle. It is important to note that the three numerators are

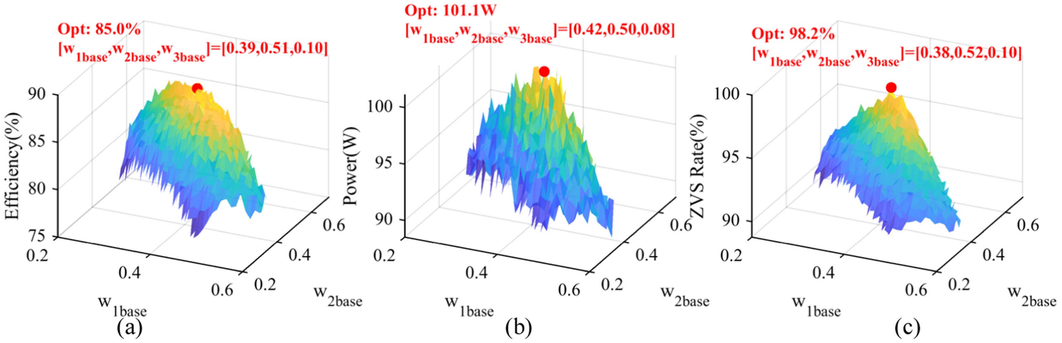

Fig. 6. Baseline-weight parameters at P_{ref}= 100 W. Efficiency (%), delivered power (W), and ZVS realization rate (%) versus ($w_{1\text{base}}$, $w_{2\text{base}}$). (a) 85.0% at [0.39, 0.51, 0.10]. (b) 101.1 W at [0.42, 0.50, 0.08]. (c) 98.2% at [0.38, 0.52, 0.10]. The adopted baseline is [0.40, 0.50, 0.10].

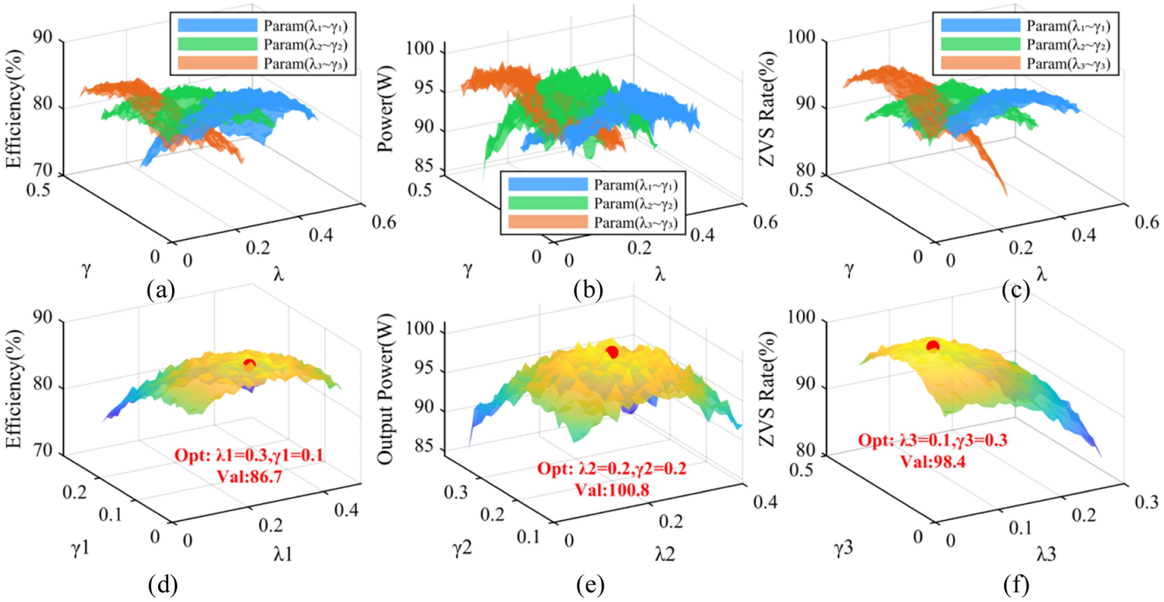

Fig. 7. Sensitivity-gain parameters with baseline weights fixed at $[w_{1\text{base}}, w_{2\text{base}}, w_{3\text{base}}] = [0.40, 0.50, 0.10]$, P_{ref}= 100 W. Panels (a)–(c) compare the effects of (λ_1, γ_1), (λ_2, γ_2), and (λ_3, γ_3) on efficiency, power, and ZVS rate. (d) $\lambda1 = 0.3$, $\gamma1 = 0.1 \rightarrow 86.7\%$ efficiency. (e) $\lambda2 = 0.2$, $\gamma2 = 0.2 \rightarrow 100.8$ W. (f) $\lambda3 = 0.1$, $\gamma3 = 0.3 \rightarrow 98.4\%$ ZVS rate.

clipped to $[0, 1]$ prior to normalization, for numerical robustness during infrequent transients because this projection will retain the intended priority shifts while also ruling out negative or arbitrarily large intermediate weights. The addition only requires $O(1)$ arithmetic per cycle and naturally accommodates the finite-candidate predictive optimization.

To render (37) operationalizable and reproducible, we conducted a simulation-based parameter design at a 100-W reference power: the results are summarized in Figs. 6 and 7. First, we swept the baseline weights under the simplex constraint $w_1(k) + w_2(k) + w_3(k)$= 1 while holding all other controller parameters fixed and computed three performance surfaces: steady-state efficiency, delivered output power, and ZVS realization rate. As shown in Fig. 6(a)–(c), the peak regions of the three surfaces lie in a narrow neighborhood, with representative optima at $[w_{1\text{base}}, w_{2\text{base}}, w_{3\text{base}}] = [0.39, 0.51, 0.10]$ for efficiency (85.0%), [0.42, 0.50, 0.08] for output power (101.1 W), and [0.38, 0.52, 0.10] for ZVS rate (98.2%). Because these maxima are tightly clustered, we select the Pareto-proximal baseline triplet $[w_{1\text{base}}, w_{2\text{base}}, w_{3\text{base}}] = [0.40, 0.50, 0.10]$, which resides within the joint plateau and therefore preserves high efficiency, near-rated power, and a high ZVS realization rate simultaneously. The local flatness around this point provides robustness to modeling mismatch and measurement noise without sacrificing performance.

With the baseline triplet fixed, we then explored how the sensitivity pairs (λ_1, γ_1), (λ_2, γ_2), and (λ_3, γ_3) modulate the same three metrics. For each pair, the remaining gains were held at their nominal values while we mapped the corresponding performance surfaces. The results in Fig. 7(a)–(c) reveal clear, smooth optima; the detailed surfaces in Fig. 7(d)–(f) indicates that the efficiency channel peaks at $\lambda_1 =$ 0.3 and $\gamma_1 =$ 0.1 with 86.7% efficiency, the power-tracking channel peaks at λ_2= 0.2 and γ_2= 0.2 with 100.8 W delivered power, and the ZVS-robustness channel peaks at λ_3= 0.1 and γ_3= 0.3 with a 98.4% ZVS realization rate. These gains are intentionally modest, so the priority shifts they induce are decisive yet not over-aggressive when coupling varies rapidly due to receiver motion. Under these selections, large $\varepsilon P(k)$ transiently raises $w_2(k)$ and relaxes $w_1(k)$ to accelerate power recovery; an asserted $I_{\text{ZVS}}(k)$ elevates $w_3(k)$ and suppresses $w_2(k)$ until the ZVS margin is restored; in nominal conditions, the weights relax smoothly toward their baselines, preserving efficiency.

We adopt $w_{1\text{base}}= 0.4$, $w_{2\text{base}}= 0.5$, $w_{3\text{base}}= 0.1$ and $\lambda_1= 0.3$, $\lambda_2= 0.2$, $\lambda_3= 0.1$, $\gamma_1= 0.1$, $\gamma_2= 0.2$, $\gamma_3= 0.3$ for (37). As evidenced in Figs. 6 and 7, these values lie within the common high-performance plateau and yield a high ZVS realization rate while maintaining near-maximal efficiency and output power at the 100-W reference.

D. Algorithm Implementation and Pseudocode

The adaptive MPC–MPPT controller runs in real time on a DSP, performing sensing, estimation, prediction, optimization, and actuation each switching cycle. At each cycle, the ADC samples the transmitter currents and output voltage/current; the load power P_{load} is computed, and the transmitter current vector is mapped to spherical coordinates to construct the state $x\ (k) = [I_{txA}(k), I_{txB}(k), I_{txC}(k), \theta(k), \varphi(k)]^T$ while the control input is the phase-shift vector $u\ (k) = [\phi_A(k), \phi_B(k), \phi_C(k)]^T$. A sensorless perturb-and-observe routine updates the mutual inductances $\{M_A, M_B, M_C\}$ using the most recent measurements and the previously applied control, thereby refreshing the prediction model for power and efficiency. Two indicators are then evaluated: the normalized power-tracking error $\varepsilon P(k)$ and a ZVS feasibility flag derived from the minimum branch current relative to a threshold Imin; a bounded scheduling law maps these indicators to normalized weights $w_1(k)$, $w_2(k)$, $w_3(k)$ to balance efficiency, regulation, and switching reliability. Around the last optimal action, a finite set of admissible phase-shift candidates is generated; for each, a short horizon N_p predicts $\{P_{\text{load}}, \eta,$ branch currents$\}$ and accumulates the cost function $J(k)$. The candidate that minimizes $J(k)$ under constraints supplies the present control move, of which only the first step is applied to the PWM; measurements and the executed action are logged to seed the next cycle. A timer/stagnation detector periodically reseeds the candidate set to avoid local minimum, ensuring robustness under rapidly varying spatial coupling. The overall algorithm is shown in Algorithm 1.

IV. EXPERIMENTAL AND SIMULATION VERIFICATION

A. Experimental Setup and System Parameters

The proposed adaptive MPC strategy for 3-D WPT systems was validated through comprehensive simulation and experimental studies using a custom-built prototype. Fig. 8 illustrates the experimental platform featuring three orthogonally arranged transmitting coils driven by independent full-bridge inverters, a movable receiving coil connected to a rectification circuit, and a digital control system implemented on a TMS320F28335 DSP. The transmitting coils are mounted on a nonmetallic frame with precisely controlled spacing to minimize mutual coupling between transmitters while maximizing the effective charging volume.

The three transmitting coils are arranged orthogonally along the x, y, and z axes, creating a cubic charging volume of $40\times40\times40\ \text{cm}^3$. The system operates at 85 kHz with up to 100 W output capability. The electrical parameters, coil parameters, and control parameters of the experimental system are summarized in Tables I–III, respectively.

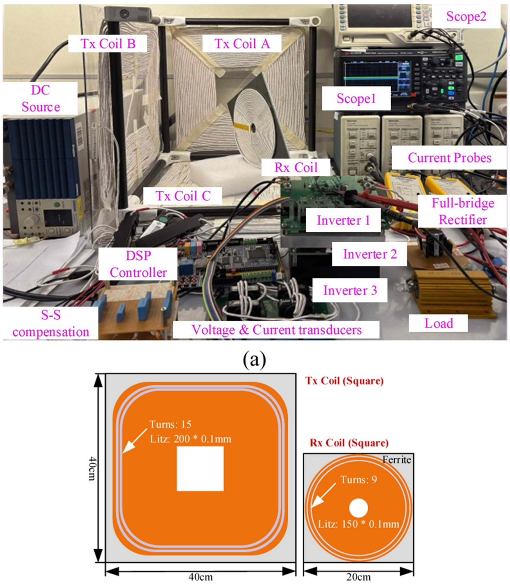

(a)

(b)

Fig. 8. Proposed platform for 3-D-WPT systems. (a) Overall experimental platform. (b) Structure of the coils.

TABLE I
ELECTRICAL PARAMETERS OF THE 3-D WPT SYSTEM

Parameter	Symbol	Value	Unit
DC input voltage	U_{dc}	12	V
Operating frequency	f	85	kHz
Transmitter resistance	R_A, R_B, R_C	0.32, 0.35, 0.33	Ω
Transmitter inductance	L_{txA}, L_{txB}, L_{txC}	23.8, 24.1, 24.5	μH
Tx compensation capacitance	C_{txA}, C_{txB}, C_{txC}	147, 145, 142	nF
Receiver inductance	L_{rx}	16.4	μH
Rx compensation capacitance	C_{rx}	215	nF
Receiver coil resistance	R_{Rx}	0.28	Ω
Mutual inductance range	M_A, M_B, M_C	0.9–4.8	μH
Output filter capacitance	C_o	270	μF
Rated output power	P_{out}	100	W

TABLE II
COIL PARAMETERS

Parameter	Transmitter Coils	Receiver Coil
Shape	Square	Circular
Outer dimension	40 cm	20 (diameter)cm
Number of turns	15	9
Wire type	Litz wire	Litz wire
Wire gauge	200×0.1 mm	150×0.1 mm
Ferrite backing	Yes (N87)	Yes (N87)
Quality factor (Q)	72–78	65

TABLE III
CONTROL PARAMETERS FOR ALGORITHM IMPLEMENTATION

Parameter	Symbol	Value
DSP clock frequency	f_{clk}	150 MHz
Control update frequency	f_{update}	200 kHz
Prediction horizon	N_p	3
Number of candidate points	N	24
Baseline efficiency weight	w_{1base}	0.4
Baseline power tracking weight	w_{2base}	0.5
Baseline ZVS weight	w_{3base}	0.1
Power tracking sensitivity coefficient	λ_1	0.3
Efficiency reduction coefficient	λ_2	0.2
ZVS reduction coefficient	λ_3	0.1
Efficiency ZVS coefficient	γ_1	0.1
Power tracking ZVS coefficient	γ_2	0.2
ZVS increase coefficient	γ_3	0.3
Minimum current for ZVS	I_{min}	1.2 A

Algorithm 1: Adaptive MPC-MPPT Implementation Flow.

```
Require: $P_{\text{ref}}, T_s, N_p$ candidate size $N$, ZVS threshold $I_{\min}$
Ensure: Next-cycle phase shifts $\{\phi_A, \phi_B, \phi_C\}$
Initialize $k \leftarrow 0$, prior control $u_{-1}$, parameters $\{M_A, M_B, M_C\}$, weights $(w_1, w_2, w_3)$.
while controller enabled do
    Measure $I_{txA}, I_{txB}, I_{txC}, V_o, I_o$; set $P_{\text{load}} \leftarrow V_o I_o$.
    $\varepsilon P(k) = |P_{\text{load}}(k) - P_{\text{ref}}|/P_{\text{ref}}$; $I_{\min}^{\text{obs}} \leftarrow \min\{|I_{txA}|, |I_{txB}|, |I_{txC}|\}$.
    $I_{\text{ZVS}} \leftarrow 1$ if $I_{\min}^{\text{obs}} < I_{\min}$ else $0$ ; $(w_1, w_2, w_3) \leftarrow$ Schedule $(\varepsilon P(k), I_{\text{ZVS}})$
    $\{M_A, M_B, M_C\} \leftarrow$ P&O_update($\{M_A, M_B, M_C\}, u_{k-1}, P_{\text{load}}$); update model $\mathcal{M}$.
    $\mathcal{U} \leftarrow \text{SeededSphereSamples}(u_{k-1}, N)$; $J_{\min} \leftarrow +\infty$; $u^\star \leftarrow u_{k-1}$
    for $u^{(n)} \in \mathcal{U}$ do
        Predict $\{P_i, \eta_i, I_i\}_{i=1}^{N_p}$ via $\mathcal{M}$ under $u^{(n)}$.
        $J(k) = \sum_{i=1}^{N_p} [w_1(k)(1-\eta(k+i)) + w_2(k)(1-\frac{P_{\text{load}}(k+i)}{P_{\text{ref}}}) + w_3(k) J_{\text{ZVS}}(k+i)]$
        if $J < J_{\min}$ then
            $J_{\min} \leftarrow J$; $u^\star \leftarrow \text{FirstControl}(u^{(n)})$.
        end if
    end for
    Apply $u^\star = \{\phi_A^\star, \phi_B^\star, \phi_C^\star\}$ to PWM; log $\{u^\star, P_{\text{load}}\}$.
    If timer expired or improvement $< \delta$, reseed $\mathcal{U}$; $k \leftarrow k + 1$.
end while
return $\{\phi_A^\star, \phi_B^\star, \phi_C^\star\}$
```

B. Power Distribution of the 3-D-WPT System

To determine the performance of the proposed adaptive control algorithm at different radial distances, the experiments were conducted by placing the receiver coil at radial distances of 10, 20, 30, and 40 cm from the reference point *O* of the transmitter. The azimuthal angle (φ) has varied between 0° and 90° in terms of the *XY*-plane projection in order to determine the receiver angles (θ) while the elevation angle was fixed at $\theta = 45°$ during the measurements. The contour plots of the measured power distributions are shown for the proportional integral controller (PI) and for the proposed adaptive MPC-MPPT strategy in Fig. 9.

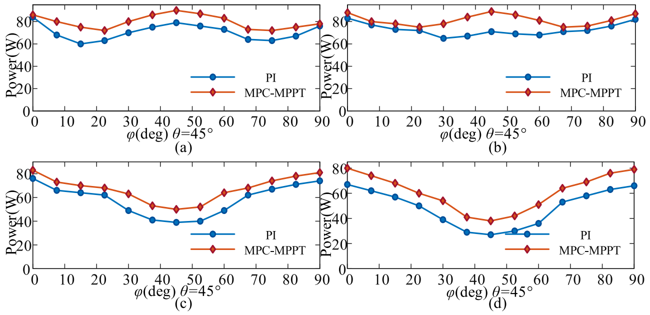

Fig. 9. Output power P_{out} versus orientation angle φ at four separation distances. (a) $r = 10$ cm. (b) $r = 20$ cm. (c) $r = 30$ cm. (d) $r = 40$ cm. Test conditions: $U_{\text{dc}} = 12$ V, $f = 85$ kHz, FSC-MPC versus MPC-MPPT.

The experimental results reveal that at shorter distances, Fig. 9(a) and (b) (e.g., $r = 10$ cm and 20 cm), the overall power transfer efficiency remains high for both methods due to stronger magnetic coupling. However, the proposed method demonstrates a clear advantage, maintaining consistently higher power delivery across the entire angular range. For $r = 10$ cm, power levels with the proposed method range between 78 and 84 W, compared to 60–78W for the conventional approach, representing approximately 15% higher power. Similarly, at $r = 20$ cm, the proposed method sustains power levels of 76–84 W, outperforming the conventional method, which yields 64–74 W.

At larger distances Fig. 9(c) and (d) (e.g., $r = 30$ cm and 40 cm), the proposed method's superiority is further pronounced. With the receiver at $r = 30$ cm, power levels using the proposed strategy remain within 52–80 W, while the conventional method experiences significant degradation, with power dropping to a range of 38–76 W. For the extreme distance of $r = 40$ cm, the proposed method maintains stable power delivery ranging from 42 to 82 W, in stark contrast to the conventional method, which suffers from power values between 28 and 74 W. Notably, the strongest performance discrepancy occurs between φ angles of 40° and 50°, where the proposed algorithm achieves up to 30% higher power transfer compared to the conventional approach. These results illustrate the robust performance of the proposed adaptive MPC-MPPT strategy. By dynamically optimizing power distribution and magnetic field alignment in real-time based on coupling conditions, it compensates for spatial variations and minimizes efficiency losses, even at extended distances. The observed stability and uniformity in power delivery highlights the proposed method's improved tolerance to angular misalignment and radial separation, making it particularly suitable for 3-D-WPT applications where receiver positioning is dynamic and variable.

C. Verification of the System's Dynamic Response.

To evaluate the dynamic performance of the proposed control strategy under realistic operating conditions, we conducted

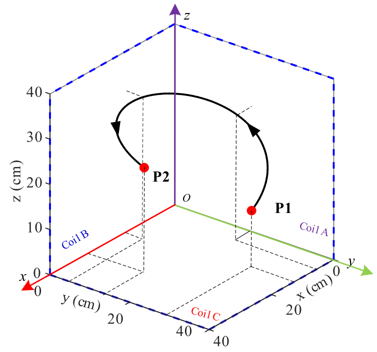

Fig. 10. Trajectory of receiver coil movement from position P1 to position P2 within the 3-D charging volume.

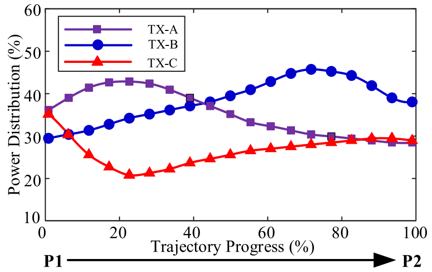

Fig. 11. Power distribution among the three transmitters as the receiver moves from P1 to P2 without the proposed control algorithm.

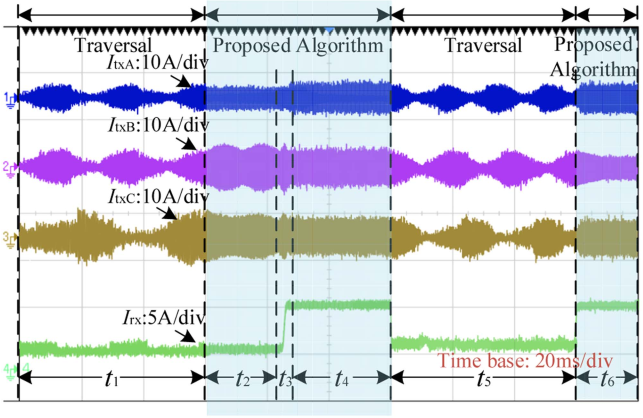

Fig. 12. Dynamic response comparison between traversal method and proposed algorithm showing transmitter currents (I_{txA}, I_{txB}, I_{txC}) and receiver current (I_{rx}) during different operating periods.

experiments with the receiver coil moving continuously through the charging volume. Fig. 10 illustrates the power distribution across the three transmitters (TX-A, TX-B, and TX-C) as the receiver moves along a defined trajectory. The horizontal axis represents the trajectory progress (%), where 0% corresponds to the starting position P1 (15, 30, 17) cm and 100% indicates the final position P2 (25, 15, 25) cm of the receiver's path. This normalized metric shows the receiver's relative position along the complete trajectory from P1 to P2.

The transition from P1 to P2 involves multiple changes in coupling conditions:

1) coupling to coil B increases as the receiver approaches the *x*-axis;
2) coupling to coil A increases as the receiver moves toward the center in the *y*-dimension; and
3) coupling to coil C decreases as the receiver rises in the z-dimension. This complex transition requires constant reorientation of the magnetic field to maintain optimal power transfer.

Prior to investigating the system's transient response characteristics, it is useful to consider the power distributions among the three transmitters when the receiver moves along the P1–P2 axis intentionally ignoring the adaptive controller under examination. Fig. 11 shows this power distribution as a percentage of total input power for each transmitter (TX-A, TX-B, and TX-C) versus percentage of progress along the P1–P2 trajectory.

The power distribution shifts significantly during movement TX-A initially dominates (reaching ∼43% at 20% trajectory progress) while TX-C drops to its minimum (∼21%). In the latter half of the trajectory, TX-B becomes the dominant transmitter (peaking at ∼46% near 75% progress). This uncontrolled power distribution leads to suboptimal efficiency and unstable power delivery, as the system lacks any mechanism to actively optimize the magnetic field direction.

To evaluate the dynamic response of our proposed algorithm, we conducted a series of experiments with specific time intervals as shown in Fig. 12. The currents in the three transmitting coils (I_{txA}, I_{txB}, I_{txC}) and the receiver coil (I_{rx}) are shown during six distinct operating periods.

1) *Verification for the static state of the receiving coil:* For time intervals, t_1 and t_2, the receiving coil was static. For time interval t_1, the proposed algorithm was "OFF"; there were fluctuations of the received current from 3.2 to 4.1 A. Then, in time interval t_2, the proposed algorithm was "ON", and the output current stabilized to a constant 3.8 A. These experimental results indicate that the proposed algorithm, very quickly, was able to achieve the maximum power point and demonstrate an advanced ability to maximize power transfer in the static state.
2) *Verification for when the receiver coil is in motion:* For time interval t_3, the receiver coil moved from P1 to P2, which created a significant change in the coupling relationship between receiver coil and transmitter coil. The proposed algorithm was able to adaptively adjust by changing the transmission currents: I_{txA} increased from 5 to 8 A, I_{txB} decreased from 10 to 9.5 A, and I_{txC} decreased from 10.8 to 8.4 A. Despite the motion, the receiver-side current, I_{rx}, achieved rapid stabilization with recorded fluctuations across all samples being below +0.3 and −0.3 A in the first experimental run. This rapid response of the algorithm was achieved in 5 ms, as shown in the data.

Continuously track the maximum power in the subsequent t_4 interval and then repeat the verification of these two processes in the t_5 and t_6 intervals.

The oscilloscopes waveforms in Fig. 13 show the transient response features of the system when the output-voltage reference steps from 20 to 30 V (10 ms/div). In the case of PI control [see Fig. 14(a)], the output voltage still shows a slow

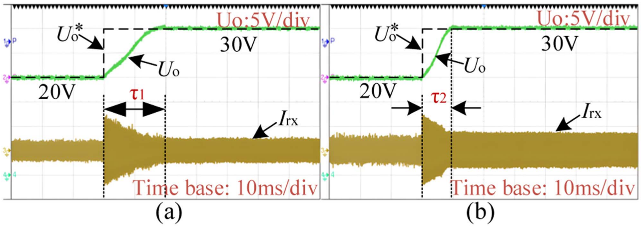

Fig. 13. Dynamic responses of output dc voltage and receiving-side current for: (a) PI Controller. (b) MPC-MPPT Controller (PI: $k_p = 0.14$, $k_i = 0.21$).

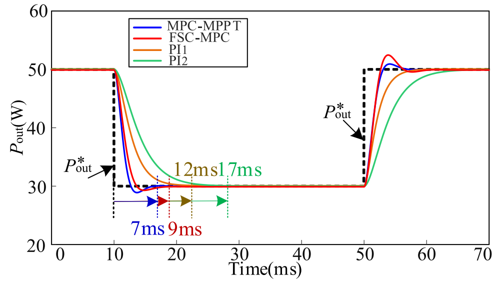

Fig. 14. Comparison of different methods with dynamic response in sudden reference output power change (PI1: $k_p = 0.14$, $k_i = 0.21$.PI2 : $k_p = 12$, $k_i = 60$).

settling time (τ_1), the current at the receiving side has large ringing, and it oscillates for some time; this may indicate a large amount of transient reactive energy exchanged. For the proposed MPC-MPPT [see Fig. 14(b)], there is a more rapid voltage transition with lower settling time ($\tau_2 < \tau_1$) without as large current transients, indicating less steady state ripple. Collectively, these results indicate that the controller can respond more rapidly to changes in the transmitter's current vector and dampen the oscillation while at the same time moving much faster to the new point of operation.

Fig. 14 shows the further quantification of the behavior under sudden output-power reference steps of around 50→30 W at 10 ms, and in the case of the opposite step 30→50 W at 50 ms, of the four controllers: The proposed MPC-MPPT performed the down-step in 7 ms, FSC-MPC performed the down-step in 9 ms, PI1 was 12 ms, and PI2 was 17 ms. The proposed MPC-MPPT down-step showed the least overshoot and the quickest settling relative to the other controllers, while the traditional MPC down-step had the largest overshot and took the longest to recover to the set point, alike, PI1 had the largest overshoot but with the longest recovery. Finally, PI2 was overdamped in down-step as it experienced no overshoot but also took the longest to settle. In summary, these results further validate the proposed controller achieves the best transient tracking, smallest power excursion, and quickest settling time across all cases.

These experimental findings indicate that the adaptive MPC-MPPT control algorithm proposed in this article performs well under static and dynamic conditions, providing a fast dynamic response while ensuring maximum power transfer.

D. ZVS Verification

Fig. 15 presents the experimental waveforms that verify the ZVS operation achieved by the proposed control strategy. The oscilloscope captures show voltage and current waveforms for all three transmitter coils and the receiver circuit during system operation.

In Fig. 15(a)–(c), the voltage waveforms and current waveforms of all three transmitter coils demonstrate clear ZVS characteristics. The voltage transitions from high to low occur precisely when the current crosses zero in the negative-to-positive direction, while transitions from low to high align with positive-to-negative current zero-crossings. Despite the different current amplitudes required by the adaptive control strategy to optimize the 3-D magnetic field distribution, all three transmitters maintain proper phase relationships between voltage and current waveforms. This phase relationship ensures that switching occurs when voltage across the MOSFET is minimized, significantly reducing switching losses.

The consistency across all transmitters demonstrates the effectiveness of the ZVS penalty term (J_{ZVS}) in the cost function, which successfully maintains the current amplitude of each transmitting coil above the critical threshold $\boldsymbol{I}_{\min}$.

The receiver waveforms also exhibit stable operation with proper resonance characteristics, indicating efficient power transfer. The smooth sinusoidal current waveforms across all coils confirm minimal harmonic distortion, which contributes to the system's high efficiency (up to 87% as demonstrated in the efficiency analysis).

In summary, the experimental findings provide evidence that the adaptive MPC-MPPT control technique presented in this article can facilitate ZVS operation for all three transmitters simultaneously as the receiver is being traveled with. This experimental result effectively reduces both switching losses and electromagnetic interference, which enhances system performance. The next section provides more details on performance evaluation, specifically efficiency.

E. System Efficiency and Power Loss Distribution Analysis

The results of the new 3-D-WPT system were assessed by paired repeated measures testing under the same conditions. In Fig. 16(a), the proposed PI (baseline) and MPC-MPPT (proposed) are summarized by the transmission distance for each pairing between 10 and 40 cm. The points denote means and error bars indicate the 95% confidence interval. As shown, the proposed method consistently demonstrates greater end-to-end efficiency, and gains presented also increase with transmission distance: +5.3% at 10 cm, +7.6% at 15 cm, +9.9% at 20 cm, +12.2% at 25 cm, +15.4% at 30 cm, +17.9% at 35 cm, and +20.0% at 40 cm. While improvements were less significant at shorter distances (10–15 cm) where coupling was strong, they became more apparent at greater distances beyond 20 cm. At $r = 40$ cm, the proposed method improves efficiency by 20.0% (95% CI shown by the error bars; paired across identical test conditions).

In Fig. 16(b), efficiency versus output power are shown at 20 and 40 cm. At 20 cm, the proposed controller supplies the sensor at 87% efficiency at the 60 W operating point, which is about a 12% absolute gain over the PI broken at the same operating point. At 40 cm, the proposed controller shows about 72% efficiency across the power range tested, which is about a 17% absolute gain at 60 W. The light-load operation (20–40 W) shows the largest

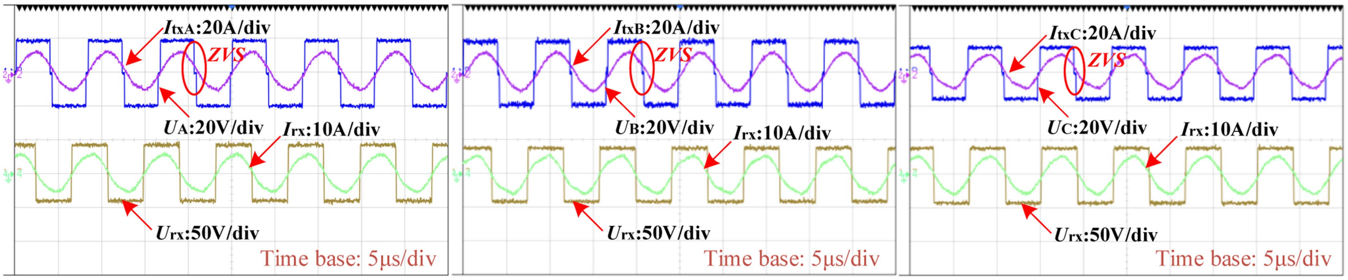

(a) (b) (c)

Fig. 15. ZVS verification: transmitter Tx voltages/currents and receiver Rx voltage/current for (a) Tx-A, (b) Tx-B, and (c) Tx-C.

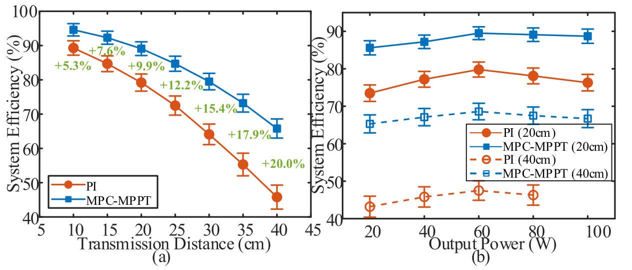

Fig. 16. System efficiency analysis of the proposed 3-D-WPT system. (a) Efficiency comparison across transmission distances. (b) Efficiency characteristics under different output power levels, error bars denote 95% confidence intervals.

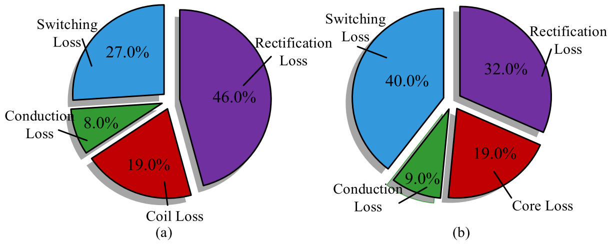

Fig. 17. Power loss distribution (a) with adaptive MPC-MPPT control, (b) with PI control.

TABLE IV
PERFORMANCE COMPARISON UNDER IDENTICAL PLANT, SAMPLING, AND TEST CONDITIONS

Metric	MPC-MPPT	PI	FCS-MPC	AIM (simulation)
η at 20 cm, 60 W	**87%**	~79%	~83%	~85%
η at 40 cm, 60 W	**~72%**	~52%	~63%	~66%
Power-Tracking 50−30 W (W)	~1.2	~3.1	~1.5	~2.0
2% settling time, 50−30 W (ms)	7ms	12ms	9ms	~10–12ms
ZVS ratio	~98–99%	~90–92%	~94–96%	~95–96%
Computation time per control cycle (μs)	5	5	4	4

percentage increases (≈15–18%) and medium (≈12–15%) and heavy loads (≈8–10%) also benefited. In both subplots, the error bars represent 95% confidence intervals calculated from paired, repeated measurements taken under the same conditions.

The integrated MPC–MPPT enhances end-to-end efficiency by

1) steering the transmit current vector toward the instantaneous MPP to maximize real power and suppress reactive,
2) enforcing ZVS via a minimum-current constraint and a penalty term to reduce switching losses, and
3) using predictive that minimize off-MPP operation during motion.

Of particular note, at $r = 40$ cm, the severe drop in magnetic coupling will be the reason that forcing the output power to 100 W will cause the input-side power devices to fail to operate properly and cause a system fault. This issue will be addressed with the further optimization of the experimental platform in future studies.

In addition, the power loss profiles of the systems with different controllers (PI and adaptive MPC-MPPT) at a transmission distance of 20 cm are investigated in Fig. 17.

The proposed method reduces switching loss from 40% to 25% by maintaining stable ZVS across the inverters, achieved through real-time phase shift control and current management. ZVS minimizes energy dissipation during state transitions by aligning voltage and current waveforms, ensuring the switches commutate at zero or near-zero voltage. This not only decreases energy loss but also mitigates thermal stress, improving overall reliability. Despite a slight increase in coil loss due to magnetic field realignment, the overall efficiency benefits from reductions in conduction, switching, and rectification losses, showcasing the effectiveness of the proposed MPC-MPPT integration in stabilizing operation and optimizing power distribution.

F. Comparative Evaluation of Advanced Controllers

To improve the baseline analysis, we compare the adaptive MPC-MPPT we propose with a well-tuned PI baseline, a finite-control-set MPC (FCS-MPC) applied on our prototype, and an adaptive impedance matching (AIM) controller we assessed through a high-fidelity simulation because of hardware considerations. All methods share the same plant, sampling, dead-time, compensation network, and protocol including static tests at 20 and 40 cm (angle 45°), stepping power 50–30W and 30–50 W, and testing a 3-D motion trajectory. Evaluation criteria will include efficiency, power-tracking RMSE, 2% settling time, ZVS ratio across the range, and per-cycle computation time. We summarize the results in Table IV.

In brief, we see that the proposed method provides the best global tradeoff-reaction under weak coupling and more extreme angle where it has the highest efficient operation while the tracking errors are consistently low and the ZVS satisfaction is near unity; the FCS-MPC provides transients that are comparable but with an increased switching loss closer to the ZVS boundary, and AIM provides strong steady-state efficiency conditions around it is tuned point but slower adaptation to rapid shifts in pose.

V. CONCLUSION

After the research and experimental validation in this article, we propose and implement a novel 3-D-WPT that combines MPC and MPPT. Through the orthogonal coil structure design and control algorithm fusion, the system demonstrates excellent power transfer performance under varying spatial coupling conditions. Mathematical models and experimental data show that the adopted system architecture and control framework can improve efficiency by about 20% at a transmission distance of 40 cm and reach a peak efficiency of 87% at 60 W output power. The stability and adaptability of the system's dynamic power transfer are significantly improved compared to conventional methods, achieving real-time response and efficient charging of mobile receiver devices. In addition, this study achieves a good balance between efficiency, power tracking accuracy and switching soft-switching conditions through an adaptive weight adjustment mechanism. The implementation of ZVS further reduces the switching loss of the system while ensuring efficient and safe operation. These features make this system important for application scenarios that require high degrees of freedom, such as mobile robots and bionic aerial vehicles.

REFERENCES

[1] H. Xiao, K. W. E. Cheng, and S. Bu, "Analytical power fluctuation suppression with reconfigurable Tx coils for dynamic inductive power transfer systems," *IEEE Trans. Power Electron.*, to be published, doi: 10.1109/TPEL.2025.3577933.

[2] L. Shuguang, Y. Zhenxing, and C. Gang, "Design and realization of high power density EV charging module," in *Proc. Chin. Control Decis. Conf.*, 2019, pp. 4909–4913, doi: 10.1109/CCDC.2019.8832920.

[3] Z. Ye and K. W. E. Cheng, "Design and validation of a multioutput wireless power transfer system using MPC controller," *IEEE Trans. Power Electron.*, vol. 39, no. 12, pp. 16065–16077, Dec. 2024, doi: 10.1109/TPEL.2024.3434516.

[4] T. Hua, M. Chen, and K. W. E. Cheng, "Magnetic power distribution using controlled permeability bypass and its multiple output investigation," *IEEE Trans. Power Electron.*, vol. 38, no. 11, pp. 14734–14746, Nov. 2023, doi: 10.1109/TPEL.2023.3302619.

[5] W. M. Ng, C. Zhang, D. Lin, and S. Y. Ron Hui, "Two- and three-dimensional omnidirectional wireless power transfer," *IEEE Trans. Power Electron.*, vol. 29, no. 9, pp. 4470–4474, Sep. 2014, doi: 10.1109/TPEL.2014.2300866.

[6] D. Lin, C. Zhang, and S. Y. R. Hui, "Mathematic analysis of omnidirectional wireless power transfer—Part-II three-dimensional systems," *IEEE Trans. Power Electron.*, vol. 32, no. 1, pp. 613–624, Jan. 2017, doi: 10.1109/TPEL.2016.2523506.

[7] C. Zhang, D. Lin, and S. Y. Hui, "Basic control principles of omnidirectional wireless power transfer," *IEEE Trans. Power Electron.*, vol. 31, no. 7, pp. 5215–5227, Jul. 2016, doi: 10.1109/TPEL.2015.2479246.

[8] Z. Zhang and B. Zhang, "Angular-misalignment insensitive omnidirectional wireless power transfer," *IEEE Trans. Ind. Electron.*, vol. 67, no. 4, pp. 2755–2764, Apr. 2020, doi: 10.1109/TIE.2019.2908604.

[9] X. Dang, P. Jayathurathnage, F. Liu, S. A. Al Mahmud, C. R. Simovski, and S. A. Tretyakov, "High-efficiency omnidirectional wireless power transfer system," *IEEE J. Emerg. Sel. Topics Ind. Electron.*, vol. 3, no. 3, pp. 403–410, Jul. 2022, doi: 10.1109/JESTIE.2022.3155365.

[10] C. Rong, X. He, Y. Zeng, C. Lu, and M. Liu, "High-efficiency orientation insensitive wpt systems using magnetic dipole coil for low-power devices," *IEEE Trans. Power Electron.*, vol. 37, no. 5, pp. 4985–4990, May 2022, doi: 10.1109/TPEL.2021.3137225.

[11] J. Shin et al., "Design and implementation of shaped magnetic-resonance-based wireless power transfer system for roadway-powered moving electric vehicles," *IEEE Trans. Ind. Electron.*, vol. 61, no. 3, pp. 1179–1192, Mar. 2014, doi: 10.1109/TIE.2013.2258294.

[12] X. Mao, J. Lin, T. Su, and Y. Zhang, "Automatic guided vehicle wireless charging with dual receiving coils for misalignment tolerance," *IEEE Trans. Circuits Syst. II, Exp. Briefs*, vol. 71, no. 1, pp. 336–339, Jan. 2024, doi: 10.1109/TCSII.2023.3304661.

[13] Z. Yan, B. Song, Y. Zhang, K. Zhang, Z. Mao, and Y. Hu, "A rotation-free wireless power transfer system with stable output power and efficiency for autonomous underwater vehicles," *IEEE Trans. Power Electron.*, vol. 34, no. 5, pp. 4005–4008, May 2019, doi: 10.1109/TPEL.2018.2871316.

[14] A. Pacini, A. Costanzo, S. Aldhaher, and P. D. Mitcheson, "Design of a position-independent end-to-end inductive WPT link for industrial dynamic systems," in *Proc. IEEE MTT-S Int. Microw. Symp.*, 2017, pp. 1053–1056, doi: 10.1109/MWSYM.2017.8058774.

[15] Z. Luo, X. Wei, M. G. S. Pearce, and G. A. Covic, "Multiobjective optimization of inductive power transfer double-D pads for electric vehicles," *IEEE Trans. Power Electron.*, vol. 36, no. 5, pp. 5135–5146, May 2021, doi: 10.1109/TPEL.2020.3029789.

[16] Y. Li et al., "Extension of ZVS region of series–series WPT systems by an auxiliary variable inductor for improving efficiency," *IEEE Trans. Power Electron.*, vol. 36, no. 7, pp. 7513–7525, Jul. 2021, doi: 10.1109/TPEL.2020.3042011.

[17] W. Li, H. Zhao, J. Deng, S. Li, and C. C. Mi, "Comparison study on SS and double-sided LCC compensation topologies for EV/PHEV wireless chargers," *IEEE Trans. Veh. Technol.*, vol. 65, no. 6, pp. 4429–4439, Jun. 2016, doi: 10.1109/TVT.2015.2479938.

[18] C. Rong et al., "Optimized design of passive array coils for high-efficiency and anti-misalignment WPT system," *IEEE Trans. Power Electron.*, vol. 39, no. 5, pp. 6504–6514, May 2024, doi: 10.1109/TPEL.2024.3365129.

[19] L. Tan et al., "Power stability optimization design of three-dimensional wireless power transmission system in multi-load application scenarios," *IEEE Access*, vol. 8, pp. 91843–91854, 2020, doi: 10.1109/ACCESS.2020.2994653.

[20] P. Raval, D. Kacprzak, and A. P. Hu, "Multiphase inductive power transfer box based on a rotating magnetic field," *IEEE Trans. Ind. Electron.*, vol. 62, no. 2, pp. 795–802, Feb. 2015, doi: 10.1109/TIE.2014.2334666.

[21] C. Rong et al., "Optimized design of opened quasi-static cavity for omnidirectional wireless charging systems," *IEEE Trans. Power Electron.*, vol. 40, no. 6, pp. 8859–8868, Jun. 2025, doi: 10.1109/TPEL.2025.3544237.

[22] S. Liu et al., "Dynamic improvement of inductive power transfer systems with maximum energy efficiency tracking using model predictive control: Analysis and experimental verification," *IEEE Trans. Power Electron.*, vol. 35, no. 12, pp. 12752–12764, Dec. 2020, doi: 10.1109/TPEL.2020.2992517.

[23] Z. Zhou, L. Zhang, Z. Liu, Q. Chen, R. Long, and H. Su, "Model predictive control for the receiving-side DC–DC converter of dynamic wireless power transfer," *IEEE Trans. Power Electron.*, vol. 35, no. 9, pp. 8985–8997, Sep. 2020, doi: 10.1109/TPEL.2020.2969996.

[24] S. Chen, W. Ding, L. Huo, X. Wu, S. Shi, and R. Hu, "Dynamic improvement and efficiency optimization of wireless power transfer systems using improved FCS-MPC and P&O methods," *IEEE Trans. Power Electron.*, vol. 38, no. 11, pp. 14702–14718, Nov. 2023, doi: 10.1109/TPEL.2023.3302614.

[25] X. Hu, Y. Wang, Y. Jiang, W. Lei, and X. Dong, "Maximum efficiency tracking for dynamic wireless power transfer system using LCC compensation topology," in *Proc. IEEE Energy Convers. Congr. Expo.*, 2018, pp. 1992–1996, doi: 10.1109/ECCE.2018.8557494.

[26] R. Mai, Y. Liu, Y. Li, P. Yue, G. Cao, and Z. He, "An Active-rectifier-based maximum efficiency tracking method using an additional measurement coil for wireless power transfer," *IEEE Trans. Power Electron.*, vol. 33, no. 1, pp. 716–728, Jan. 2018, doi: 10.1109/TPEL.2017.2665040.

[27] N. Kang, H. Qin, R. Ma, C. H. T. Lee, M. Liu, and C. Ma, "Magnetic field projection and current phase control in a 2-D planar transmitting coil array," *IEEE Trans. Power Electron.*, vol. 39, no. 9, pp. 10623–10637, Sep. 2024, doi: 10.1109/TPEL.2024.3403094.

[28] M. Dong, M. Li, J. Zhou, Z. Wu, and L. Li, "3-D sensing intermediate coils for receiver position identification and power enhancement in WPT system," *IEEE Trans. Power Electron.*, vol. 40, no. 6, pp. 8812–8823, Jun. 2025, doi: 10.1109/TPEL.2025.3533012.

Zhenxing Ye (Student Member, IEEE) received the B.Sc. degree in automation from Huangshan University, Huangshan, China, in 2018, and the M.Sc. degree in control engineering from Xi'an Polytechnic University, Xi'an, China, in 2022. He is currently working toward the Ph.D. degree in power electronics with the Department of Electrical and Electronic Engineering, Faculty of Engineering, Hong Kong Polytechnic University, Hong Kong.

In 2021, he was with the Laboratory for Artificial Intelligence in Design as a Research Assistant. His current research interests include inductive/wireless power transfer, electric vehicles, object detection, autonomous driving, and artificial intelligence.

Ka Wai Eric Cheng (Fellow, IEEE) received the B.Sc. degree in electrical and electronic engineering and the Ph.D. degree in power electronics from the University of Bath, Bath, U.K., in 1987 and 1990, respectively.

Before joining The Hong Kong Polytechnic University, Hong Kong, in 1997, he was with Lucas Aerospace, London, U.K., as a Principal Engineer. He is currently a Professor with the Department of Electrical Engineering, Faculty of Engineering, at The University of California, Merced, CA, USA.

He has authored or coauthored more than 400 articles and seven books. His research interests include all aspects of power electronics, motor drives, electromagnetic interference, electric vehicles, battery management, and energy saving.

Dr. Cheng was the recipient of the Institution of Electrical Engineers Sebastian Z De Ferranti Premium Award in 1995; the Outstanding Consultancy Award in 2000; the Faculty Merit Award for Best Teaching from The Hong Kong Polytechnic University in 2003; the Faculty Engineering Industrial and Engineering Services Grant Achievement Award in 2006; the Brussels Innova Energy Gold Medal with Mention in 2007; the Consumer Product Design Award, in 2008; the Electric Vehicle Team Merit Award of the Faculty, in 2009; the Eco Star Award in 2012; the Gold Prize at Seoul International Invention Fair in 2015; the iCAN Gold Medal at Canada for contribution in active suspension in 2016; the Gold Award of HK Innovation and Technology for contribution in body integrated supercapacitor for vehicles in 2017; the Geneva Invention Expo Silver Medal for contribution in e-Antilock braking systems in 2021; and TechConnect 2023 and Geneva Invention Siler Award 2024 for contributions to Ammonia Electric Vehicles.

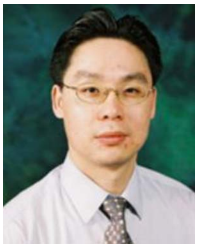

Ka Wing Cha Chan (Member, IEEE) received the B.Sc. (Hons.) and Ph.D. degrees in electronic and electrical engineering from the University of Bath, U.K., in 1988 and 1992, respectively. He is currently a senior lecturer in the Department of Electrical and Electronic Engineering of the Hong Kong Polytechnic University. His general research interests include power system stability, analysis and control, power grid integration, security, resilience and optimization, demand response management, etc.

Siu Wing Or received the B.Sc. (Hons.), M.Phil., and Ph.D. degrees in engineering physics from The Hong Kong Polytechnic University (PolyU), Hong Kong, in 1995, 1997, and 2001, respectively.

He was a Teaching Company Associate, a Research Electronic Engineer, and a Senior Research Electronic Engineer with ASM Pacific Technology Ltd., Hong Kong, from 1995 to 2001. He was a Postdoctoral Research Fellow with the Mechanical and Aerospace Engineering Department, University of California at Los Angeles, Los Angeles, CA, USA, for one and a half years. He joined PolyU as a Lecturer, in 2002. He is currently a Professor, the Director of Smart Materials and Systems Laboratory, and the Director of Electrical Protection and High Voltage Coordination Laboratory with the Department of Electrical Engineering, PolyU. He has authored or coauthored more than 300 publications, including 2 professional book chapters, more than 210 SCI journal articles, more than 100 international conference papers, in addition to the award of 43 patents. His research interests include smart materials and devices in the bulk, micro and nanoscale, the AIoT sensing and electrical condition monitoring, energy harvesting, storage and management, and electromagnetic absorption and shielding.